LOSS OF ENERGETIC BEAM IONS DURING TAE INSTABILITIES

H.H. DUONG, W.W. HEIDBRINK, E.J. STRAIT*,
T.W. PETRIE*, R. LEE*, R.A. MOYER**, J.G. WATKINS+
Physics Department,
University of California,
Irvine, California,
United States of America

ABSTRACT. Toroidicity induced Alfvén eigenmodes (TAE) are observed in the DIII-D tokamak when energetic beam ions (~75 keV) are used to destabilize the mode. Measurements of the neutron emission indicate that up to 70% of the injected power is lost during strong TAE activity. Measurements of the poloidal distribution of fast ion losses suggest that the losses are greatest near the vessel midplane. Fast ion losses in discharges with combined fishbones and TAE bursts are 1.5 to 2 times greater than losses in fishbone discharges without TAE activity. The scaling of fast ion losses with MHD mode amplitude exhibits no threshold in the mode amplitude, suggesting that mode particle pumping is the dominant loss mechanism.

1. INTRODUCTION

In recent years considerable progress has been made in the development of fusion energy, with tokamak experiments rapidly approaching ignition conditions. To sustain ignition in a burning plasma, most of the alphas produced in deuterium-tritium (DT) fusion reactions must be confined long enough to heat the bulk plasma. Collective alpha driven instabilities, such as toroidicity induced Alfvén eigenmodes (TAE), are of concern for future tokamak devices since they can induce anomalous alpha losses. Furthermore, future devices such as the international thermonuclear experimental reactor (ITER) may use ~1 MeV neutral beams for external heating and neutral beam current drive. These energetic beam ions may also destabilize TAE modes, thereby possibly reducing heating and current drive efficiency. Moreover, if the fast ion losses are localized, they could damage the first wall. Prior experiments on both DIII-D [1] and TFTR [2] have shown that super-Alfvénic beam ion populations can destabilize TAE modes in a deuterium plasma; therefore, it is both prudent and cost effective to study TAE modes in a deuterium machine before the construction of a DT reactor. The first reports from DIII-D [1] and TFTR [2, 3] have concentrated on identification of the TAE modes and given an overview of their properties. Recently, papers have considered the radial mode structure in TFTR [4], the stability [5, 6] and real frequency [7] of TAE modes in DIII-D, the non-linear saturation of the instability [8], initial studies of fast ion losses in TFTR [9] and the effect of TAE modes on the confinement of MeV ions in DIII-D [10].

This paper reports the first detailed study of the effect of TAE instabilities on the confinement of energetic beam ions. Measurements of the neutron emission and of the power flux to the wall monitor the losses of fast ions during TAE activity. Up to 70% of the fast ions are lost during strong TAE activity. The losses are concentrated near the vessel midplane. The data also suggest that combined TAE and fishbone [11] activity are more effective in expelling fast ions than either instability alone. The scaling of fast ion losses with MHD mode amplitude exhibits no threshold in the mode amplitude, suggesting that mode particle pumping is the dominant loss mechanism.

2. BACKGROUND

2.1. Destabilization of TAE modes by energetic ions

In normal high field ($B_T \gtrsim 1.5$ T) operating regimes, TAE modes are stable in DIII-D; however, with the proper plasma conditions, the modes are readily destabilized. In a tokamak plasma, ideal magneto-hydrodynamic (MHD) modes may be excited in the

Permanent affiliations:
* General Atomics, San Diego, California, United States of America.
** University of California, Los Angeles, California, United States of America.
+ Sandia National Laboratories, Albuquerque, New Mexico, United States of America.

presence of pressure gradients created by circulating fast ions. The combination of the pressure gradient and the magnetic curvature induces a diamagnetic drift ω_{*f} that, if sufficiently large, may excite Alfvén waves via inverse Landau damping. Normally, Alfvén waves are strongly damped; however, finite toroidicity can induce gaps in the Alfvén continuous spectrum [12] where TAE modes may be destabilized. The fast ion drive term (neglecting finite gyroradius effects) is of the form (see Refs [13–16])

$$\gamma_f = \beta_f \left(\frac{\omega_{*f}}{\omega_0} - \frac{1}{2} \right) F(x) \quad (1)$$

where β_f is the local fast ion beta, ω_{*f} is the fast ion diamagnetic frequency evaluated at the average energy of the fast ions, x is the ratio of the Alfvén speed to the parallel component of the fast ion speed and $\omega_0 = v_A/2qR$ is the real frequency of the TAE mode ($v_A = B/\sqrt{\mu_0 n_i m_i}$ is the Alfvén speed, q is the safety factor and R is the major radius). The quantity F is related to the fraction of the distribution function that resonates with the mode and is maximized for $v_\parallel \simeq v_A$. The fast ion drive (Eq. (1)) is opposed by various damping mechanisms, including electron Landau damping [13, 15, 16], collisional electron damping [17, 18], damping on kinetic Alfvén waves [18], ion Landau damping [15] and continuum damping [19, 20]. Instability requires an intense fast ion population (large β_f), a steep fast ion pressure gradient ($\omega_{*f} \gtrsim \omega_0/2$) and a large number of resonant particles. Thus, experimentally, it is advantageous to maximize both the injected beam power and the parallel component of the beam ion velocity to create a super-Alfvénic fast ion population. For a more complete treatment of the stability of TAE modes in DIII-D, we refer the reader to Ref. [6].

2.2. Description of the observed instabilities

In the experiments conducted for this study, up to 20 MW of 75 keV deuterium neutral particles are injected into deuterium plasmas. The density of the background plasma is moderate ($\bar{n}_e = (2\text{–}6) \times 10^{13}$ cm^{-3}), in order to minimize v_A but maximize β_f. The fast ion profile is peaked near the centre of the plasma with a central fast ion beta of ~15% [1, 6], which is approximately a factor of three greater than the expected alpha particle beta for ITER [21]. The toroidal field ranges from 0.6 to 1.4 T with $I_p = 0.4\text{–}1.2$ MA. At 1.0 T, the ratio of the beam ion gyroradius to the plasma minor radius (ρ_f/a) is $\sim 8 \times 10^{-2}$; this value is similar to that of the alphas in ITER where $\rho_\alpha/a \sim 6 \times 10^{-2}$ [21]. In DIII-D, TAE activity can be excited over a wide range of plasma configurations (single null divertor, double null divertor and inner wall limiter) and in both low confinement mode (L mode) and high confinement mode (H mode) plasmas. However, since the optimum condition for destabilizing TAE modes is a high injected beam power in a low field plasma, it is desirable to keep the plasma in the L mode to avoid the beta limit.

Under the plasma conditions described, bursts of high frequency oscillations identified as TAE activity are observed on magnetic probes and soft X ray detectors [1]. These high frequency bursts of Mirnov activity are usually accompanied by two types of low frequency MHD modes. One type consists of semi-continuous oscillations with toroidal mode numbers ranging from $n = 1$ to $n = 4$ (possibly tearing modes). The other low frequency modes are bursts of $n = 1$ activity (fishbones and sawteeth). In plasma discharges with fishbones [11] and sawteeth, high frequency TAE bursts usually accompany low frequency bursts (often during the growth phase of the fishbone or of the sawteeth) and sometimes occur during the quiescent period between these low frequency bursts. A sudden drop in neutron emission usually (but not always) coincides with high frequency bursts. In cases where the high frequency burst is synchronous with a sawtooth, the magnitude of the neutron drop can be as large as 38%, whereas isolated high frequency bursts cause only 3–7% drops in the neutron emission. Fourier decomposition of the magnetic signals reveals spectral peaks ranging from 50 to 210 kHz during the high frequency bursts. The high frequency toroidal mode numbers range from $n = 1$ to $n = 10$, with several toroidal modes usually excited. Each toroidal mode consists of coupled poloidal modes. The observed high frequency modes in DIII-D usually peak between the $q = 1$ surface (the location of which is given by $r/a \sim 0.4$ [1]) and the $q = 2$ surface with an amplitude (at the wall) of up to $\tilde{B}_\theta/B_T \sim O(10^{-4})$. Measurement of the soft X ray emission suggests plasma displacements of O(1 mm) during TAE bursts [1].

3. EXPERIMENTAL METHOD

3.1. Diagnostics

The primary diagnostics used to monitor the fast ion behaviour in these experiments are neutron scintillators and foil bolometers. Mirnov coils are used to identify the instabilities and to measure the mode amplitude and toroidal mode number. A midplane fast reciprocating Langmuir probe is also used to monitor the outer edge

of the plasma, and high frequency magnetic probes are used to monitor RF activity near the edge of the plasma.

The main diagnostic used on DIII-D to identify TAE and other MHD instabilities is a comprehensive set of internal magnetic (Mirnov) probes. In addition to measuring the local magnitude of the poloidal field, the DIII-D magnetic probes are capable of detecting magnetic fluctuations over a wide range of plasma conditions with bandwidths of approximately 250 kHz. The MHD mode numbers (n and m) are determined from the phase differences between probes positioned at different poloidal and toroidal locations. For experiments with the purpose of studying TAE instabilities, the data from the probes are archived at 500 kHz, which allows us to examine magnetic fluctuations up to 250 kHz.

The neutron emission is measured with a plastic scintillator accompanied by a zinc sulphide (ZnS) scintillator to discriminate against hard X rays. The electronics for the detectors is similar to that of TFTR [22]. The ZnS scintillator measures moderated neutrons and is less sensitive to the hard X rays produced from runaway electrons and Cerenkov radiation. However, because it measures moderated neutrons, the ZnS scintillator has a slower response time than its plastic counterpart. The intrinsic response time is ~ 100 ns for the plastic scintillator and ~ 100 μs for the ZnS scintillator. However, the actual response time of the plastic scintillator is limited to ~ 50 μs by the electronics. Both scintillators are cross-calibrated with a set of ^{3}He and BF_3 neutron counters to infer the absolute neutron flux.

During the vessel vent in the autumn of 1991, a set of foil bolometers was installed on the outer walls of DIII-D to measure directly the fast ion losses during TAE instabilities. Foil bolometers were better suited for this study (instead of simply looking at the vessel wall) because we needed greater sensitivity. Surrounding the main 180° limiter are three Inconel foils (with a thickness $\delta = 0.25$ mm and a radius $r = 22.5$ mm) that are recessed 2.4 mm beneath the surface of the protective graphite tiles (see Fig. 1). These foils are viewed by an infrared (IR) camera located approximately 45° toroidally from the limiter. At about the same toroidal location an identical Inconel foil is placed on a divertor baffle plate located near the bottom of the vessel. This fourth foil is viewed by a second IR camera that is often used to monitor the divertor region from above. The location of these four foil bolometers was originally chosen to provide us with a four point poloidal measurement of the escaping fast ion flux; however, because of hardware constraints, we were not able to monitor the foils above the midplane and the poloidal measurement was limited to only three locations. Inframetric model 525 monitoring cameras with a radiation detection capability of 3–5 μm [23] were used. The detected radiation is converted to an electrical signal by a mercury-cadmium-telluride detector. The signal is then processed to transmit a television image (with ~ 30 ms time resolution) of the behaviour of the foil surface temperature. The data are archived on a VHS type video tape and are subsequently digitized.

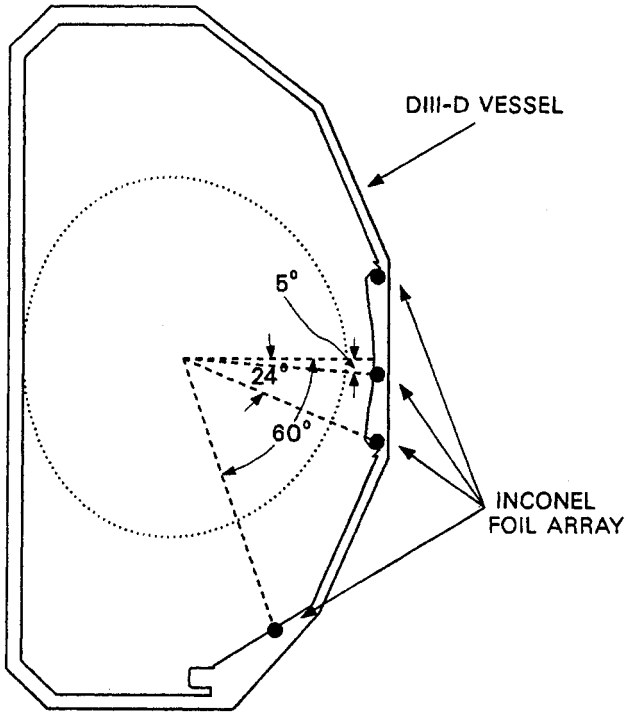

FIG. 1. Poloidal projection of the DIII-D vessel and the poloidal locations of the Inconel foil bolometer array. Also shown is the plasma boundary of a $\kappa = 1.2$ TAE discharge.

In addition to measurements with foil bolometers, a local measurement of the fast ion flux can be extracted from ion saturation current measurements obtained with a fast reciprocating Langmuir probe near the vacuum vessel wall. The probe strokes 15 cm into position (approximately 2.5 m behind the limiter) in 70 ms, dwells there for 30 ms and retracts in another 70 ms. During the plunge, the data are sampled at a frequency of up to 2 MHz. The probe ion collection electrode is a small rounded graphite cylinder of diameter 2 mm and length 4 mm. The collector is biased to -200 V with respect to the vessel potential.

Ion cyclotron emission (ICE) measurements are made with a set of RF probes patterned after the PDX high frequency magnetic coils used to study magnetic instabilities [24]. Each ICE probe is made up of two single

turn coils that are wound in opposite senses, with the centre conductors connected to their respective Inconel outer shields to complete the circuit. For our experiment, two ICE probes (one is oriented to intercept the poloidal flux and the other intercepts the toroidal flux) are used. The RF signal from each single turn coil in each coil pair is terminated just outside the vacuum vessel at a differential power combiner to reduce electrostatic pick-up. In addition, the power combiner acts as a DC safety break. From the power combiner, the signal goes through an eight way splitter, with each of the eight channels filtered at different bandwidths and then rectified and amplified before being archived. The passive bandpass filters are centred at 10, 25, 35, 45, 55, 65, 75 and 85 MHz, each with 10 MHz bandwidths. The data are archived at 5 kHz.

3.2. Data analysis and interpretation

As discussed in Section 4, the data from the neutron detectors, from the foil bolometers, from the fast reciprocating Langmuir probe and from the ICE probes all indicate that beam ions are ejected from the hot centre of the plasma. To infer fast ion losses from the neutron emission, we assume that beam-target reactions predominate and that the injected beam ions thermalize classically in the absence of MHD activity. For most DIII-D plasma discharges, beam-target fusion reactions are dominant, with the possible exception of VH mode discharges, where thermonuclear fusion reactions can be significant, and low density discharges, where beam-beam fusion reactions can be large. For the plasma conditions described in this paper, we estimate that the beam-target fusion reactions constitute more than 70% of the total neutron emission, with beam-beam fusion reactions making up the remaining neutron emission. The losses are inferred from the impulsive drops in neutron emission ΔI_n at the MHD bursts and from the average value of the emission $\bar{I}_n$.

The first method for evaluating fast ion loss from the neutron emission makes use of the model developed to interpret the neutron emission during the fishbone instability [25]. The model interprets the impulsive drops in neutron emission as the result of the ejection of energetic particles from the plasma centre and assumes that the averaged energetic ion confinement time takes the form

$$\langle \tau_c \rangle = \frac{T_{MHD}}{-\ln[1/(1 - \Delta I_n/I_n)]} \qquad (2)$$

where T_{MHD} is the interval between MHD bursts and $\Delta I_n/I_n$ is the fractional drop in neutron emission (see Fig. 2(a)). For a discharge with MHD bursts of different amplitude the averaged confinement time is approximately

$$\langle \tau_c \rangle \simeq \frac{\Delta t}{\sum \Delta I_n/I_n}$$

where the summation is over all the drops in neutron emission in the time interval Δt. Since this model neglects beam-beam fusion reactions, it underestimates $\langle \tau_c \rangle$ by a factor of $(1 + 2\zeta)/(1 + \zeta)$, where ζ is the ratio of beam-beam to beam-target emission [25]. In our

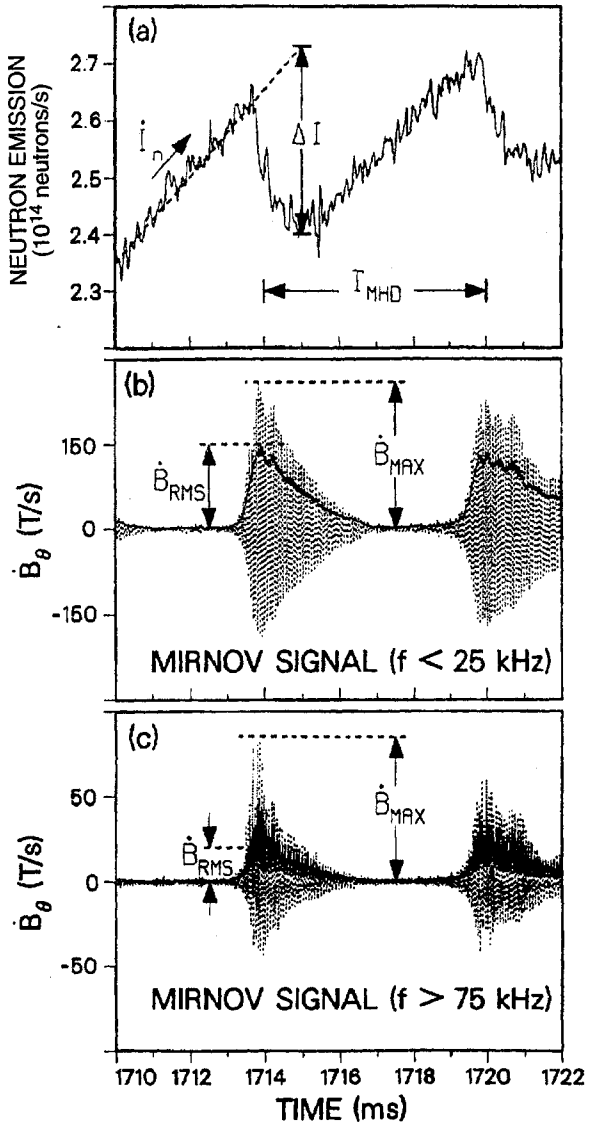

FIG. 2. Time evolution of (a) the DD neutron emission, (b) the low pass filtered Mirnov signal and (c) the high pass filtered Mirnov signal for a typical discharge with TAE activity. Also shown are symbolic definitions of various parameters used in the TAE database.

case, $\langle \tau_c \rangle$ is underestimated by $\lesssim 30\%$. Another assumption of the model is that the sudden reduction in the neutron emission is the result of fast ion loss rather than of a redistribution of the fast ion population. Theoretically, a flattening of the fast ion profile can cause a rapid reduction of the observed neutron emission. However, TAE discharges in DIII-D have rather flat thermal density profiles [1]; thus, considerable transport of fast ions is required to produce any significant reduction in the neutron emission. Moreover, the assumption of fast ion loss is supported by edge measurements (as discussed below). From the averaged confinement time the fast ion loss rate is simply $\nu_{loss} \sim 1/\langle \tau_c \rangle$. The loss of injected beam power is related to ν_{loss} as

$$P^{a}_{loss} = P_{inj}\left(\frac{\tau_s}{\nu^{-1}_{loss} + \tau_s}\right) \tag{3}$$

where τ_s is the fast ion slowing down time and P_{inj} is the injected beam power. Finally, another useful parameter for analysing fast ion loss is the instantaneous energetic beam ion confinement time [25]

$$\tau_c(t) = \frac{I_n(t)}{\dot{I}_n(t_0) - \dot{I}_n(t)} \tag{4}$$

where $\dot{I}_n(t)$ is the slope of the neutron emission and t_0 is a time prior to the onset of the MHD burst.

The second method for estimating energetic ion loss using neutron emission takes advantage of the fact that the fast ion stored energy W_f depends on the number of fast ions N_f in the plasma. In predominantly beam–plasma fusion reactions, the neutron emission is proportional to the number of energetic beam ions, $I_n \simeq N_f n_d \langle \sigma v \rangle_{bp}$ (n_d is the deuterium density and $\langle \sigma v \rangle_{bp}$ is the fusion reactivity). Since Z_{eff} is relatively small for the discharges presented here ($Z_{eff} \lesssim 2$), $n_d/n_e \simeq$ constant. This allows us to express the fast ion stored energy in terms of the neutron emission as $W^{exp}_f = k\bar{I}_n/n_e$, where k is some constant, $\bar{I}_n$ is the averaged neutron emission and n_e is the electron density. Comparison between W^{exp}_f and the classically expected value W^{class}_f yields the relation

$$P^{b}_{loss} = P_{inj}\left(1 - \frac{W^{exp}_f}{W^{class}_f}\right) \tag{5}$$

where P^{b}_{loss} is the beam power loss, P_{inj} is the injected beam power and

$$W^{class}_f = \frac{P_{inj}\tau_{se}}{2}\left\{1 + \frac{2}{3}\left(\frac{v_c}{v_f}\right)^2 \times \left\{\frac{1}{2}\ln\left(\frac{(v_f + v_c)^2}{v_f^2 - v_f v_c + v_c^2}\right) - \sqrt{3}\left[\frac{\pi}{6} + \tan^{-1}\left(\frac{2v_f - v_c}{\sqrt{3}v_c}\right)\right]\right\}\right\} \tag{6}$$

In the expression for W^{class}_f, τ_{se} is the Spitzer slowing down time, v_c is the critical speed where the drag on the thermal ions equals the drag on the thermal electrons, and v_f is the fast ion speed. Equation (6) is the stored energy for a fast ion slowing down distribution (neglecting energy diffusion above the injection energy and the contribution of the half and third energy components to the distribution function; the contribution of the half and third energy components constitutes less than 5% of the distribution function). Basically, this second method estimates fast ion losses by comparing the measured average neutron emission with the classically predicted value and assumes that any deficit is due to anomalous fast ion loss; the first method (Eq. (3)) estimates fast ion losses from the sudden drops in the neutron emission.

The calculation of the escaping fast ion flux on the foil bolometers is made on the basis of the variation in the measured surface temperature of the foils as a function of time. Owing to the fact that the foils are only 0.25 mm thick, we can assume that the surface temperature of the foils is approximately the same as their bulk temperature and that both radiative and conductive losses on the foils are negligible for short plasma discharges. With these assumptions, the total power flux (background plasma and fast ion flux) is simply (see Ref. [23])

$$Q = \frac{d}{dt}[\rho c(T_B) T_B \delta] \approx \frac{d}{dt}[\rho c(T_s) T_s \delta] \tag{7}$$

where ρ is the foil mass density (g/cm^3), δ is the foil thickness (cm), T_s and T_B are the foil surface and bulk temperatures, respectively, and $c(T)$ is the specific heat as a function of temperature (J·g^{-1}·K^{-1}). The radiation from the plasma is measured by a bolometer array consisting of thermistor detectors; this background plasma radiation is subtracted from the total flux measured by the bolometer foil to yield the escaping fast ion flux. Another source of background interference is reflection. Reflection is accounted for by examining the area surrounding the foil. Any excessive noise due to reflection (typically $\lesssim 45\%$ of the total

measured signal) can then be subtracted from the measured signal of the foil.

The optical train (OT) is calibrated using a commercially available black body emulator with a temperature range of 300–1300 K. The entire OT is removed from the vessel and reassembled in a test laboratory with all the geometrical parameters preserved. We first use the black body source to calibrate the OT over the temperature range of interest (300–500 K) with the same electronics as used during the experiment. Next, we determine the emissivity of each of the four Inconel foils by comparing the emission of the black body source as reflected from the foil with that from a mirror. Using the relation

$$\epsilon = 1 - \frac{S_{\text{foil}}}{S_{\text{mirror}}} \tag{8}$$

(ϵ is the foil emissivity, and S_{foil} and S_{mirror} are the observed signals reflected from the foil and the mirror, respectively) we can estimate the emissivity of each Inconel foil. With a knowledge of the sensitivity of the OT to a black body source and the emissivity of each foil, we are now able to obtain the efficiency of each foil over the full temperature range of interest.

The data from the Mirnov coils are analysed by a Fourier decomposition code to provide the cross-power spectrum of the signals and the mode numbers of the field perturbations m and n. In our analysis, the $\dot{B}$ signal is digitally filtered to distinguish the high frequency Mirnov activity ($f \gtrsim 75$ kHz) from the low frequency activity ($\lesssim 25$ kHz). To facilitate the identification of any systematic behaviour, the amplitudes of the oscillations are then entered into the database as $\dot{B}_{\text{max}}$ and $\dot{B}_{\text{RMS}}$ for both the high frequency signal and the low frequency signal (Figs 2(b) and (c)).

4. RESULTS

The data collected for this study sample all available DIII-D discharges up to the spring of 1992 with Mirnov coil and neutron data that were archived at 500 kHz. A database containing representative MHD activity from each discharge (approximately 500 events) was formed. The section begins with results from the neutron emission, followed by measurements of the power flux to the vessel wall using foil bolometers. The results from other measurements that correlate with the neutron data are also presented.

4.1. Neutron data

The principal concern with TAE instability is the ejection of energetic particles caused by these modes. Using the database, we first perform a consistency check on the methods used to calculate the fast ion losses (Section 3.2). Comparison of the beam power loss calculated using Eq. (5) with the loss calculated from Eq. (3) yields good agreement (Fig. 3). For a few plasma discharges, we use a third method to estimate the lost power. The transport code ONETWO [26] computes the expected fast ion energy (assuming no losses), and the thermal stored energy is obtained from the profile measurements of T_e, T_i and Z_{eff}. The expected stored energy is compared with the actual stored energy inferred from the equilibrium code EFIT [27]. Any deficit is attributed to fast ion losses. The ONETWO/EFIT calculations are in good agreement with the two neutron methods (Fig. 3). Figure 3 indicates that up to 10 MW (or 70%) of injected power is lost during intense MHD activity.

An example of the time evolution of the neutron emission, the beam energy and the beam power loss

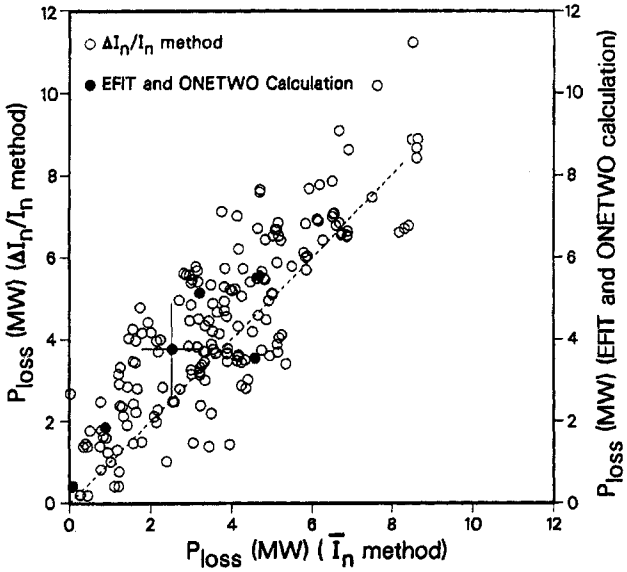

FIG. 3. Methods of deducing fast ion losses from the neutron emission are compared for consistency. The ordinate is the loss of injected beam power derived from the averaged neutron emission $\bar{I}_n$. The abscissa represents the loss of injected beam power derived from the drop in the neutron emission ΔI_n (shown as open circles) and the loss of injected beam power calculated by the equilibrium code EFIT [27] and by the transport code ONETWO [26] (represented by solid circles). The error bars represent the relative uncertainty of the data. All three independent methods of estimating fast ion loss are in good agreement.

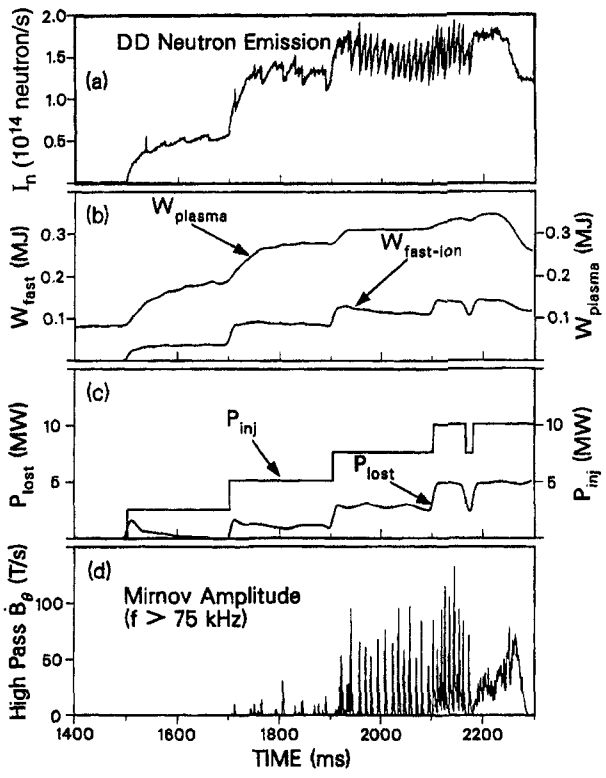

FIG. 4. Time evolution of (a) the DD neutron emission, (b) the plasma stored energy and the fast ion energy, (c) the injected beam power and the time average (~ 40 ms) lost beam power and (d) the high frequency Mirnov amplitude for a plasma discharge with ~50% loss of beam power during TAE activity. The plasma stored energy is derived from an equilibrium fit, and $W_{fast\ ion}$ and P_{lost} are calculated using Eqs (6) and (5), respectively. A large loss of beam power is observed after 1900 ms when large high n *activity develops. The transition from the three beam phase to the four beam phase at 2100 ms results in a shorter time between MHD bursts and large beam power loss. At 2180 ms, a transition from fishbones to* n = 2 *activity occurred. The experiments were conducted at* $B_T = 0.8$ *T,* $I_p = 0.67$ *MA and* $\bar{n}_e = 3 \times 10^{13}$ *cm*$^{-3}$.

during TAE activity is shown in Fig. 4. Also shown in the same figure is the time evolution of the mode amplitude of a high pass filtered Mirnov signal ($\dot{B}_\theta$), the plasma stored energy and the injected beam power. In this particular example, the injected beam power increases in stairstep fashion from one beam (~2.5 MW) to four beams (~10 MW). During the one beam phase, the plasma is relatively stable to high frequency activity, and the loss of beam power is negligible. As additional beam power is added, the actual fast ion beta increases and high frequency activity begins to develop. During the two beam phase, the drops in the neutron emission increase in size as more fast ions are ejected from the plasma, resulting in larger losses of the injected beam power. By the three beam phase, the size of the drops in neutron emission reaches its maximum amplitude and the loss in beam power is approximately 30%. The transition from three beams to four beams results in smaller values of τ_{MHD} and even greater loss of injected beam power (~50%) because of the shorter periods between MHD bursts.

The tendency for losses to increase with increasing classical fast ion beta is generally observed in our dataset. In Fig. 5, the loss of beam power, calculated from the averaged neutron emission, is plotted versus the classically predicted value $\beta_f^{c\ell}$. Figure 5 shows that up to 70% of the injected beam power is lost during violent TAE activity. The figure also establishes a systematic correlation between large beam power loss and high $\beta_f^{c\ell}$ in our experiments. In this figure, MHD events that exhibit TAE behaviour are represented by solid circles, whereas those without are represented by open circles. Clearly, in both cases, fast ion losses are observed at high $\beta_f^{c\ell}$; however, it appears that the adverse effect of high $\beta_f^{c\ell}$ is greater for discharges with TAE activity.

As we can see from results mentioned thus far, the fast ion beta plays an important role in the behaviour of the fast ions. Therefore, it is not surprising that one of the most striking results from our data is indeed

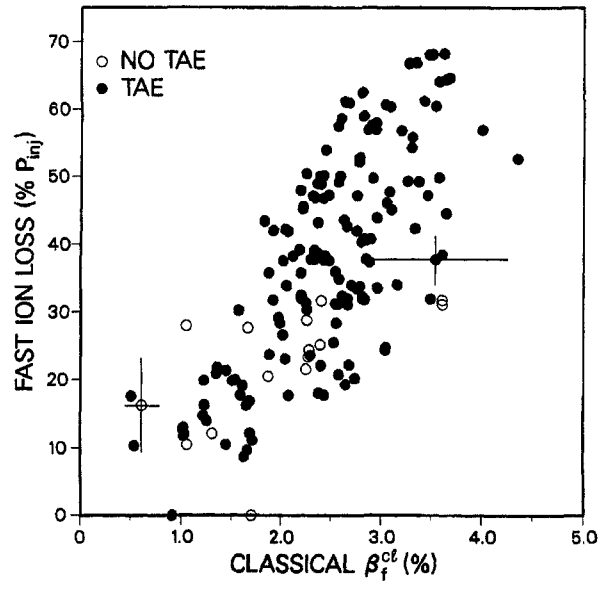

FIG. 5. Energetic ions lost (expressed as a fraction of the injected beam power) during MHD activity as a function of the classically predicted fast ion beta. The data represented by open circles are events without high frequency Mirnov activity and those represented by solid circles are events with high frequency TAE activity. The error bars represent the relative uncertainty of the data.

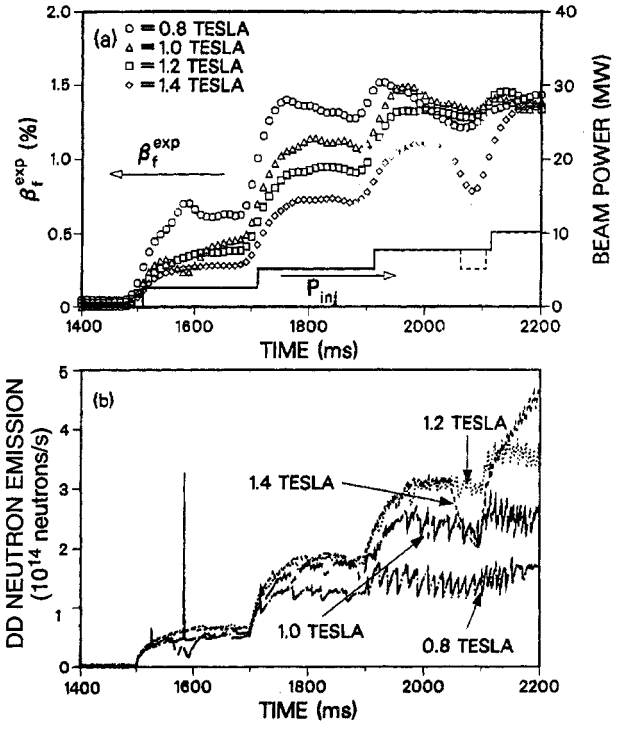

FIG. 6. (a) Time evolution of fast ion β_f^{exp} from a toroidal field scan showing evidence of β_f^{exp} saturation. (b) Time evolution of the DD neutron emission for the same discharges.

the effect of TAE instabilities on the experimentally measured fast ion beta (β_f^{exp}). As the toroidal field is lowered during a B_T scan with similar injected beam power, we observe a behaviour where the neutron emission tends to saturate at a lower level owing to what appears to be 'β_f^{exp} clamping'. In this series of plasma discharges, the beams were increased in stair-step fashion up to 10 MW, while B_T was scanned from 0.8 to 1.4 T. It appears that the reduction in neutron emission at low field is the result of saturation of β_f^{exp}, as indicated in Fig. 6(a). After β_f^{exp} reaches the saturation level (about 1.5%), high n instabilities develop and the beam ions are quickly ejected from the plasma centre. As we increase the injected beam power by stacking more beams, the size of the neutron drop at each MHD event increases (Fig. 6(b)), resulting in greater fast ion losses, thus preventing the neutron emission from exceeding the saturation level.

Earlier, in Section 2.2, we noted that high frequency TAE bursts are usually correlated with fishbones and sawteeth. Figure 7 is a typical example of such behaviour. If we examine each burst closely, however, we can see that each event exhibits a different behaviour. At 2141 ms, there is a fishbone burst (indicated by the low pass Mirnov signal) with little high frequency activity (indicated by the high pass Mirnov signal). This combination of moderate size fishbones ($\tilde{B}_\theta/B_T \sim 1.2 \times 10^{-3}$) and weak high frequency bursts ($\tilde{B}_\theta/B_T \sim 3.0 \times 10^{-6}$) causes a slight reduction in the neutron emission ($\Delta I_n/I_n \sim 5\%$). At 2148 ms, an isolated high n ($\tilde{B}_\theta/B_T \sim 1.9 \times 10^{-5}$) burst develops with no low frequency MHD activity. Here, the drop in neutron emission is negligible ($\Delta I_n/I_n \lesssim 1\%$). Another combination of fishbone and high frequency activity is seen at 2152.5 ms with a slightly stronger high frequency activity ($\tilde{B}_\theta/B_T \sim 2.1 \times 10^{-5}$). With this combination, the drop in neutron emission is significantly higher ($\Delta I_n/I_n \sim 12\%$) than that for the events at 2141 and 2148 ms. An even larger drop in the neutron emission ($\Delta I_n/I_n \sim 25\%$) occurs at 2157.5 ms, where we see a combination of a sawtooth ($\tilde{B}_\theta/B_T \sim 1.4 \times 10^{-3}$) and high frequency activity ($\tilde{B}_\theta/B_T \sim 3.4 \times 10^{-5}$). Although the amplitude of the low frequency $n = 1$ field perturbation is comparable with the perturbations in the previous fishbones, the drop in the neutron emission is greater, owing to the larger high frequency activity. Through Fourier decomposition of the Mirnov signal, the most strongly excited mode in these high frequency bursts is identified as an $n = 6$ TAE mode. In this discharge, the size of the drop in neutron emission depends more strongly on the magnitude of the high frequency activity than on the amplitude of the low frequency activity.

The trends illustrated in Fig. 7 are generally observed in plasmas with TAE activity. In Fig. 8, the drop in the neutron emission is plotted versus the RMS high frequency mode amplitude ($\dot{B}_{RMS}$) derived from the Fourier decomposition of the Mirnov signal. In this set of data, all events in the database having large low frequency activity are eliminated, to reduce any possible contamination from low frequency harmonics during Fourier decomposition. The data indicate that, as the high frequency mode amplitude increases, the drop in the number of neutrons also increases almost linearly. In contrast, no systematic trend was observed between the fast ion loss and the low frequency mode amplitude. On the other hand, larger losses are usually observed at bursts with combined low and high frequency activity than for either instability considered individually. In general, fast ion losses in discharges with combined fishbones and TAE bursts are 1.5 to 2 times greater than losses in fishbone discharges without TAE activity. However, this behaviour is true only for discharges with $\tau_d > 125$ μs. (Here, τ_d is the exponential decay time of the low frequency Mirnov burst.) In sawtooth-like events with $\tau_d < 125$ μs, fast ion losses in discharges with combined sawteeth and TAE activity

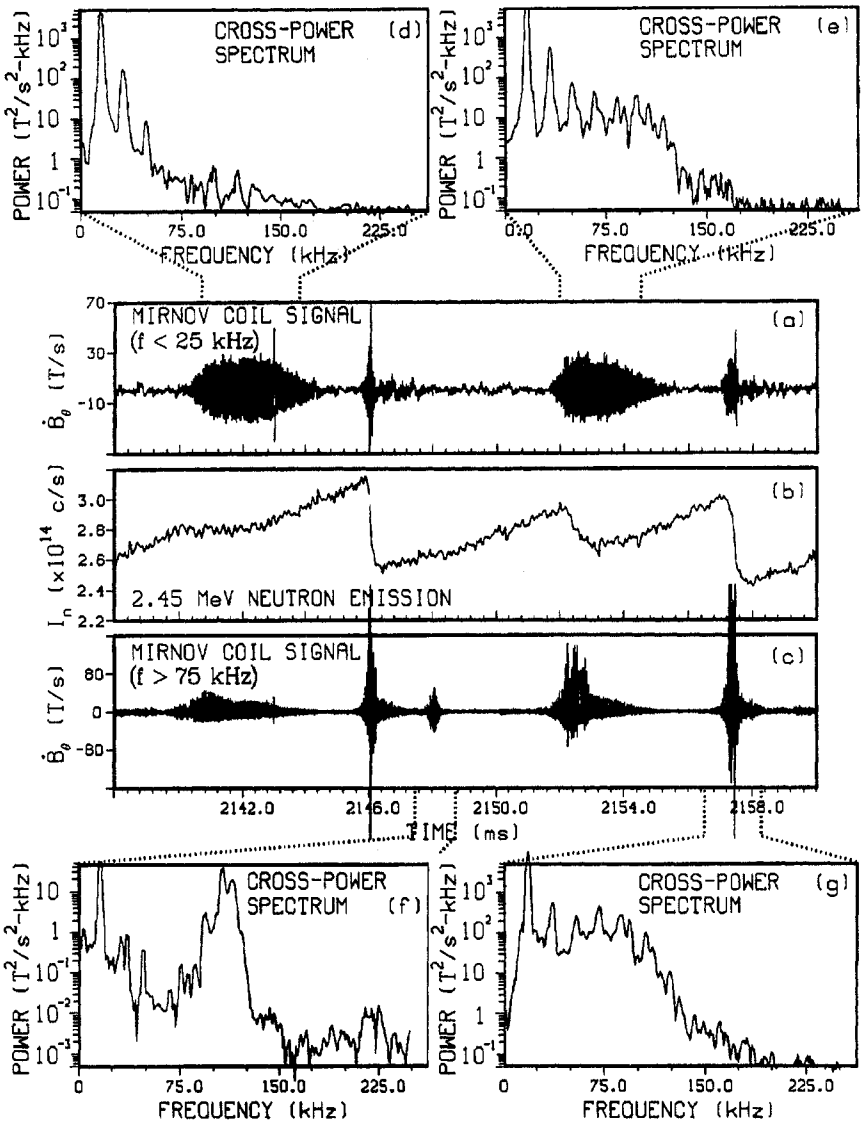

FIG. 7. Time evolution of (a) the low pass filtered Mirnov signal, (b) the DD neutron emission and (c) the high pass filtered Mirnov signal for a discharge exhibiting low frequency n = *1 Mirnov activity and high frequency TAE activity. Also shown are magnetic cross-power spectra for each type of MHD event. Part (d) shows a fishbone burst with weak TAE activity, (e) shows another fishbone burst with similar amplitude but stronger TAE activity, causing a larger drop in the neutron emission, (f) shows a TAE burst with little low frequency Mirnov activity and (g) shows a sawtooth with strong TAE activity. The experiments were conducted at* $B_T = 1.0$ *T,* $I_p = 0.6$ *MA,* $\bar{n}_e = 3 \times 10^{13}$ *cm*$^{-3}$ *and* $P_{inj} = 10$ *MW.*

are roughly equal to those in sawtooth discharges without TAE activity.

Another correlation between fast ion losses and the magnitude of the high frequency magnetic fluctuation is observed in the scaling of the instantaneous fast ion confinement time with the TAE mode amplitude. In Fig. 9, we plot the instantaneous fast ion confinement (Eq. (4)) versus the amplitude of the high frequency magnetic fluctuation ($\dot{B}_\theta$) for an event where TAE instabilities predominate. A simple power fit of the data yields the scaling

$$\tau_c \propto (\dot{B}_\theta)^{-1.03 \pm 0.21} \tag{9}$$

for this particular example. The measured TAE frequency in the laboratory frame changes by $\lesssim 10\%$; thus, any variation in τ_c is probably due to $\tilde{B}_\theta$.

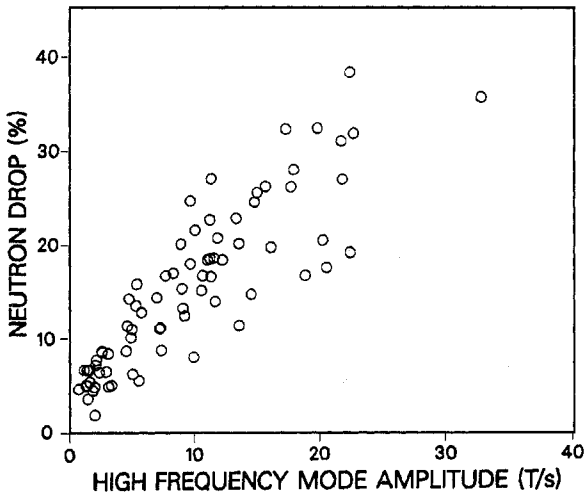

FIG. 8. Fraction of fast ions lost during TAE activity ($\Delta I_n/I_n$) as a function of the RMS amplitude (calculated by Fourier decomposition) of the high frequency (f > 75 kHz) magnetic fluctuation. In the figure, MHD events with large low frequency amplitudes are eliminated to prevent any possible contamination from low frequency harmonics during the Fourier decomposition.

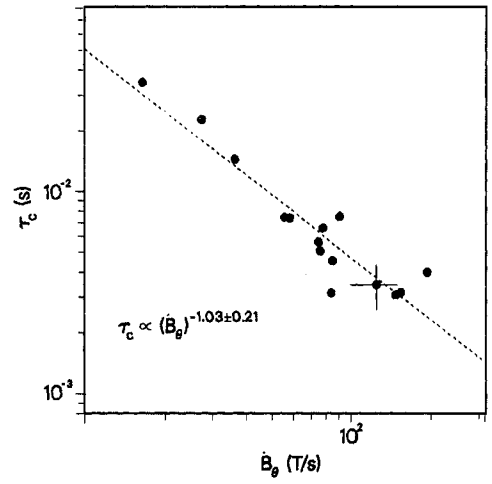

FIG. 9. Fast ion instanteneous confinement time plotted versus TAE mode amplitude ($\dot{B}_\theta$) for a discharge where TAE activity predominates. A power fit yields the relation $\tau_c = 5.5 \times 10^{-1} (\dot{B}_\theta)^{-1.03 \pm 0.21}$. The error bars represent the relative uncertainty of the data.

Figure 9 suggests that the fast ion loss rate is linearly proportional to the high frequency mode amplitude.

Most of the neutron data shown above are from MHD bursts with both TAE activity and low frequency Mirnov activity. Usually, the high frequency activity is coupled with the low frequency activity. However, we also observe discharges with only TAE activity that have appreciable fast ion losses. One such example is shown in Fig. 10. This discharge has the usual TAE signatures in the range of 70–120 kHz with a maximum mode amplitude at the toroidal mode number $n = 5$. The discharge exhibits very weak low frequency Mirnov activity that appears to be an $n = 2$ mode with a frequency of 16 kHz. Approximately 57% of the fast ion power is lost (as estimated from the average neutron emission). In this example, it is clear that the degradation in fast ion confinement is predominantly the result of TAE activity and not merely a fishbone effect.

Finally, there appears to be no systematic correlation of fast ion loss with $\beta_T q$ as previously observed during fishbone instabilities [24, 25]. Also, we observe no correlation of fast ion behaviour with β_N, β_T, I_p, the plasma elongation (κ) or the magnetic shear.

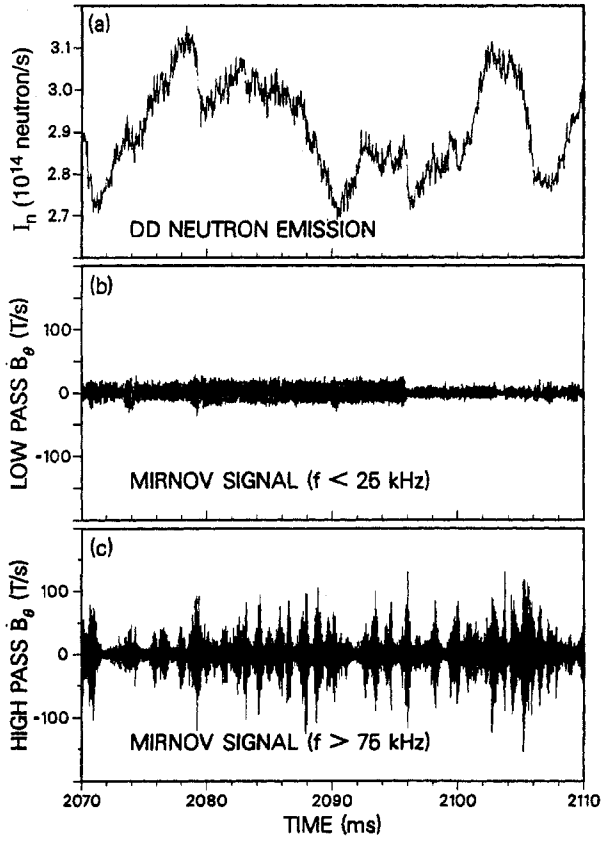

FIG. 10. Time evolution of (a) the DD neutron emission, (b) the low pass filtered Mirnov signal and (c) the high pass filtered Mirnov signal for a TAE discharge with weak low frequency Mirnov activity. Approximately 57% of the injected beam power is lost during the instability. The experiments were conducted at $B_T = 1.0$ T, $I_p = 0.6$ MA, $\bar{n}_e = 3 \times 10^{13}$ cm^{-3} and $P_{inj} = 20$ MW.

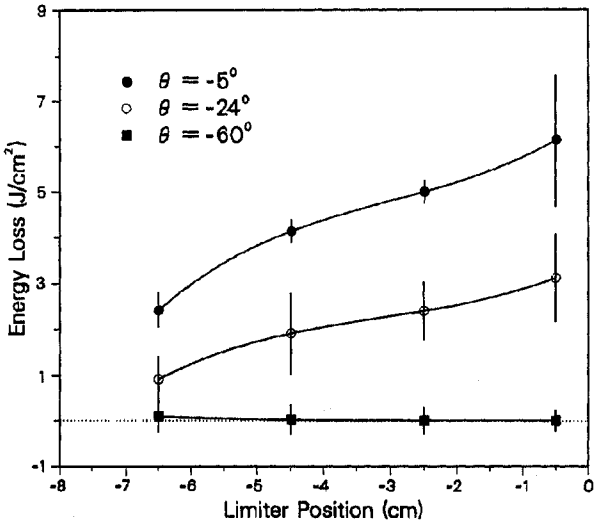

FIG. 11. Energy loss to the vessel wall plotted versus the limiter position during a limiter scan. The limiter was moved from its start-up position at $\Delta R = R_{limiter} - R_{wall} = -0.5$ *cm inside the first wall to* $\Delta R = -6.5$ *cm inside the first wall in 2 cm increments. The data shown are taken from three poloidal locations. The data represented by solid circles are taken from the midplane foil* ($\theta \sim -5°$), *the data represented by open circles are taken from a foil at the poloidal angle* $\theta \sim -24°$ *and the data represented by solid squares are taken from the* $\theta \sim -60°$ *location. The background plasma radiation is subtracted from the measured signal to show only the fast ion contribution. The error bars are the standard deviation of several time slices within a plasma discharge. The experiments were conducted at* $B_T = 0.9$ *T,* $I_p \simeq 0.42$ *MA and* $\bar{n}_e = 3 \times 10^{13}$ *cm*$^{-3}$.

4.2. Foil bolometer data

Measurement of the power flux at the first wall serves two purposes: to confirm that fast ions are ejected from the plasma (as suggested by the neutron measurements) and to assess the poloidal distribution of the fast ion losses. The best bolometer data are from a sequence of low field ($B_T = 0.9$ T), nearly circular ($\kappa \simeq 1.2$), discharges with strong TAE activity ($P^b_{loss}/P_{inj} \simeq 30\%$) and relatively short beam pulses (300 ms). The inner wall was used as the limiter for these discharges, and a relatively large outer gap of 10 cm between the plasma and the foils was employed. During the sequence, a large outer limiter (73 cm high by 25 cm wide) that was opposite the foil bolometers (180° away toroidally) was inserted into the plasma scrape-off region as an obstacle. On successive, nominally identical, discharges the position of the limiter was varied to study the effect of the obstacle on the detected heat flux. The measured heat fluxes at three different poloidal positions are shown in Fig. 11. For the data presented here, the background plasma radiation has been subtracted from the signal to yield only the fast ion contribution to the measured flux. The data show that, as the limiter is moved in past the first wall, the measured energy loss is reduced. With the limiter moved in to the maximum allowable position (owing to the high heat flux of these TAE discharges) at

$$\Delta R = R_{\text{limiter}} - R_{\text{wall}} = -6.5 \text{ cm}$$

the measured signal from the midplane foil is over a factor of two smaller than that with the limiter fully retracted ($\Delta R \simeq -0.5$ cm inside the first wall). Figure 11 also shows that more energy is deposited near the vessel midplane than below the midplane; this behaviour is observed in both circular and elongated discharges (Fig. 12). (The ∇B drift is downward for these conditions.)

During the limiter scan, we also ran high field ($B_T = 1.4$ T) 'control' plasma discharges with the TAE activity suppressed. The control discharges not only serve as comparison discharges but also as a verification of the background subtraction. Foil bolometer data from the high field discharges are compared with the low field discharges for the TAE activity in Table I. Three of the four discharges have similar low frequency activity with $\tilde{B}_\theta^{RMS}/B_T \sim O(10^{-4})$. However, the high frequency activity in low field discharges is 3 to 10 times stronger than that in high field discharges. Both the neutron and the foil bolometer data indicate a greater fast ion loss in discharges with a strong TAE activity (Table I).

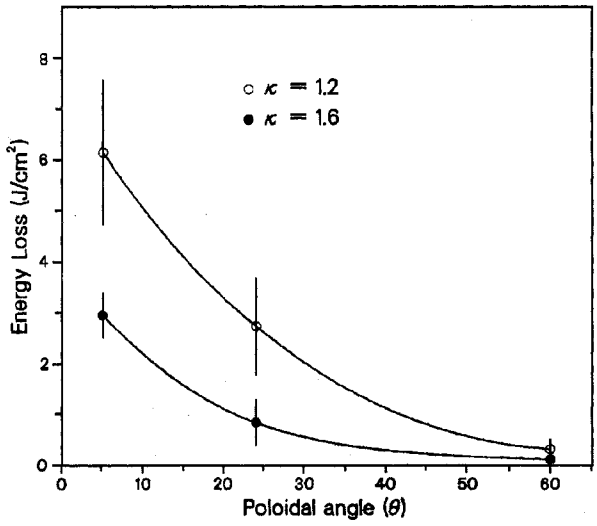

FIG. 12. Deposition of energy loss at different poloidal locations for a $\kappa = 1.2$ *discharge (represented by the open circles) and for a* $\kappa = 1.6$ *discharge (represented by the solid circles). More energy is deposited near the midplane in both discharges.*

TABLE I. COMPARISON OF NEUTRON AND FOIL BOLOMETER DATA

	MHD activity[a]		Energy loss	
B_T (T)	$\tilde{B}_\theta^{RMS}/B_T$ (<50 kHz)	$\tilde{B}_\theta^{RMS}/B_T$ (50–250 kHz)	Neutrons[b] (J)	Midplane foil[c] (J/cm^2)
0.9	3.8×10^{-4}	3.5×10^{-5}	5.0×10^5	6.2 ± 1.4
0.9	1.6×10^{-3}	2.1×10^{-5}	3.5×10^5	2.9 ± 0.9
1.4	2.4×10^{-4}	6.9×10^{-6}	3.9×10^4	1.2 ± 0.8
1.4	3.4×10^{-4}	3.8×10^{-6}	8.6×10^3	0.3 ± 0.2

[a] $\tilde{B}_\theta^{RMS}/B_T$ values are averaged over 20 ms time intervals during maximum TAE activity.
[b] Energy loss calculated from the reduction in the neutron emission.
[c] Energy loss calculated from the power flux at the midplane foil bolometer.

4.3. Correlations with other measurements

An unexpected indication of the effect of fast ion losses on the vessel components during TAE activity occurred in the early stages of the experiment when optical components of the charge exchange recombination (CER) diagnostic were damaged. Figure 13 shows the reflectivity of the midplane CER mirror before and after the first TAE plasma discharge. In the figure, the mirror reflectivity is normalized to another mirror that looks at the same location but from above the vessel. Before the first series of plasma discharges with TAE activity, the relative reflectivity of the mirror was about 30%. The relative reflectivity then dropped rapidly as we began performing the TAE study. Subsequent analysis showed that the mirror was coated with graphite. Reductions in reflectivity correlate with discharges that have a total fast ion energy loss (inferred from the neutrons) in excess of 5 MJ. We attribute the reduction in reflectivity to overheating of graphite tiles in discharges with intense fast ion losses. Figure 13 shows a strong correlation between the reduction in the mirror reflectivity and the onset of the TAE experiment, providing us with the first evidence of damage to vessel components during TAE activity. In addition, the position of the damaged mirror also suggested that the losses occurred near the midplane, as was later confirmed by heat flux measurements of the vessel walls (Section 4.2).

The observed fast ion losses inferred from the neutron emission also correlate with the signal from the midplane fast reciprocating Langmuir probe. An example of the time evolution of the ion saturation current (I_{sat}) from the Langmuir probe in a divertor plasma discharge with TAE activity is shown in Fig. 14(d). In this discharge, measurements of the I_{sat} current were performed with the Langmuir probe retracted approximately 10 cm behind the last closed flux surface to minimize interference from the plasma scrape-off region. Also plotted in Fig. 14 are the neutron emissivity and the filtered magnetic fluctuation signals. In this particular sequence, the neutron emission rises steadily to its peak at $I_n = 4.7 \times 10^{14}$ neutrons/s and begins to level off at the onset of MHD activity. At 2198 ms, both the high and the low frequency Mirnov signals increase in amplitude, with the high frequency signal reaching its maximum value at 2198.8 ms. The I_{sat} signal also peaks at 2198.8 ms and the reduction in the neutron emission (which is proportional to the total fast ion loss) is then also greatest. In contrast, the low frequency signal does not peak until 2200.0 ms. The correlation with the neutron emission and the relatively large distance from the edge plasma suggest that the I_{sat} current signal is dominated by charge deposition from escaping fast ions. With this assumption, we can interpret each I_{sat} spike in Fig. 14(d) as a burst of escaping fast ions to the outer walls of the vessel. The I_{sat} signal appears to be modulated by both the low frequency and the high frequency MHD activity. However, the I_{sat} signal follows the high frequency Mirnov signal more closely. This example of a clear correlation

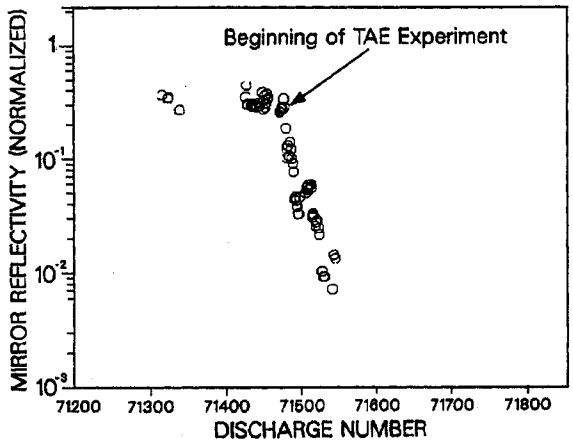

FIG. 13. Evidence of first wall component damage as a result of fast ion loss during TAE activity. The ordinate is the ratio of the transmission of a mirror located near the outer wall midplane to another mirror located near the top of the vessel. Both mirrors view the same plasma volume. The transmission of the midplane mirror was reduced to almost zero after the first two days of TAE experiments.

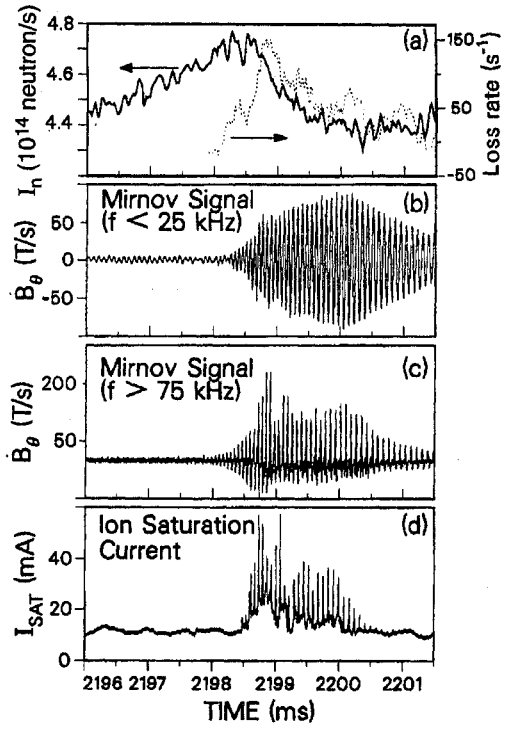

FIG. 14. Time evolution of (a) the DD neutron emisson and the fast ion loss rate calculated using Eq. (4), (b) the low pass filtered Mirnov signal, (c) the high pass filtered Mirnov signal and (d) the ion saturation current (I_{sat}) from the midplane fast reciprocating Langmuir probe positioned ~10 cm from the plasma boundary. The I_{sat} signal is modulated by both the low frequency and the high frequency Mirnov signals but follows the high frequency signal more closely. The experiments were conducted at $B_T = 0.9$ T, $I_p = 0.7$ MA, $\bar{n}_e = 3 \times 10^{13}$ cm^{-3} and $P_{inj} = 10$ MW.

between the I_{sat} signal and the TAE activity is not prevalent in our data. In plasma discharges during limiter operation, the temporal evolution does not agree as well with the neutron emission and the modulation of the signal at the MHD frequencies is weaker. We speculate that these I_{sat} signals contain contributions from both fast ions and the scrape-off plasma. It is when we produce a divertor plasma with a large outer gap that we are able to see I_{sat} bursts with minimal interference from the edge plasma density fluctuation.

Modulation of the I_{sat} signal by the Mirnov activity is also evident when we examine the cross-power spectrum of the two signals. In Fig. 15, the cross-power spectrum between I_{sat} and the magnetic signals is calculated by Fourier decomposition. From the figure, we can clearly see two distinct peaks in the spectrum, a low frequency peak at ~17 kHz and a high frequency peak at ~100 kHz, but the coherence between the Mirnov signal and the I_{sat} signal is much better at ~100 kHz than at lower frequencies.

Ion cyclotron emission bursts also correlate with fast ion losses during TAE experiments. A typical example of such behaviour is illustrated in Fig. 16, where the time evolution of the neutron emission and the ICE signal are plotted. In general, ICE bursts are observed only during events composed of multiple MHD modes (high frequency modes and low frequency modes) that result in a large rapid reduction ($\Delta I_n/I_n \gtrsim 15\%$) in the neutron emission. However, it is possible that our detectors were not sensitive enough to detect ICE bursts during MHD events with neutron drops of $< 15\%$. From Fig. 16, there appears to be almost no delay in the ICE signal in relation to the neutron drops. In addition, ICE bursts are often seen at the fundamental ion cyclotron frequency and at higher harmonics. Figure 17 shows the ICE during TAE activity in various frequency bands. As is evident from the figure, the ICE spectrum peaks at a higher harmonic, a behaviour that is generally observed for ICE data with good spectra. As discussed in Section 5, these ICE bursts further support the hypothesis that fast ions are expelled to the edge of the plasma by the MHD activity.

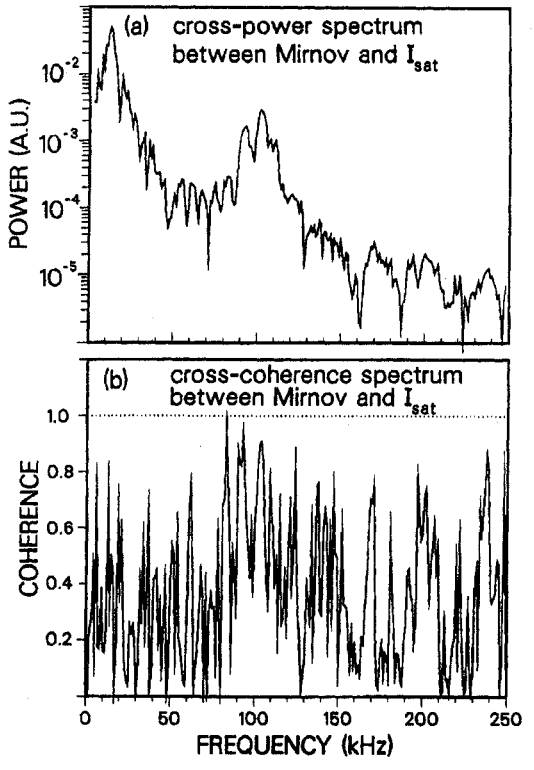

FIG. 15. (a) Cross-power spectrum between the I_{sat} signal and the Mirnov signal. The spectrum shows a clear high frequency peak at ~100 kHz. (b) Cross-coherence spectrum between the same signals.

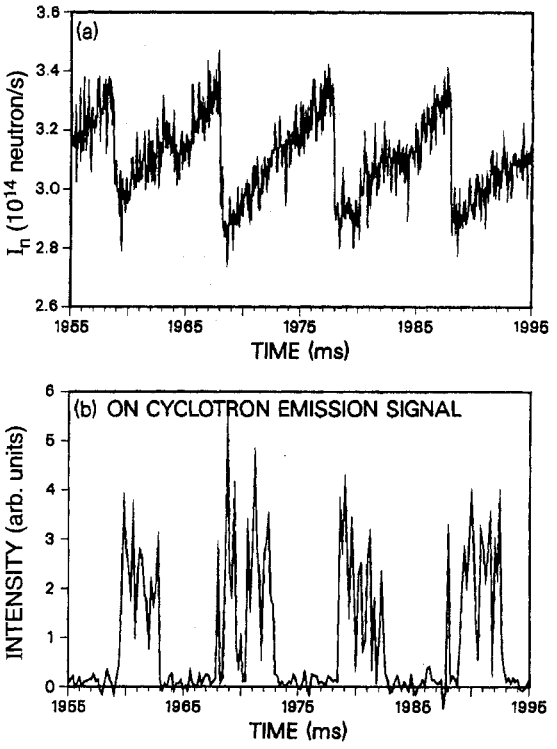

FIG. 16. Time evolution of (a) the DD neutron emission and (b) the ion cyclotron emission for a discharge with TAE activity. Note that ICE bursts occur only when there is a large drop in the DD neutron emission (usually ≳15%) and there is almost no delay in the ICE signal after the neutron drops. The fundamental ion cyclotron frequencies are ~8.4 and ~5.8 MHz at the centre and at the edge of the plasma, respectively. Here, the data are processed using a spectrum analyser with the centre frequency set at 16.8 MHz. The bandwidth of the spectrum analyser is set at 300 kHz.

5. DISCUSSION

Two volume averaged measurements (of the neutron emission and the stored energy) and four edge measurements (of the heat flux, the damaged CER optics, the ion saturation current and the ICE) all indicate that beam ions are expelled from the plasma by intense TAE activity. Quantitative estimates suggest that as much as 70% of the injected power or up to 10 MW is lost. At the midplane, the inferred power flow is ~30 W/cm^2.

In principle, some reduction in neutron emission can occur owing to the redistribution of beam ions within the plasma. The foil bolometer measurements confirm that at least part of the reduction in neutron emission at TAE bursts is due to actual losses of fast ions. For the first entry in Table I, the energy deposited in the foil is 6.2 ± 1.4 J/cm^2. From the measured poloidal distribution (Fig. 11), we estimate that beam ions are lost in a poloidal band 40–60 cm wide. Since TAE modes propagate toroidally, it is reasonable to assume that the losses are uniform toroidally ($2\pi R_{foil} \simeq 1440$ cm). Thus, the measured heat flux implies a total energy loss of approximately (3–6) × 10^5 J, which is in reasonable agreement with the loss inferred from the neutron emission.

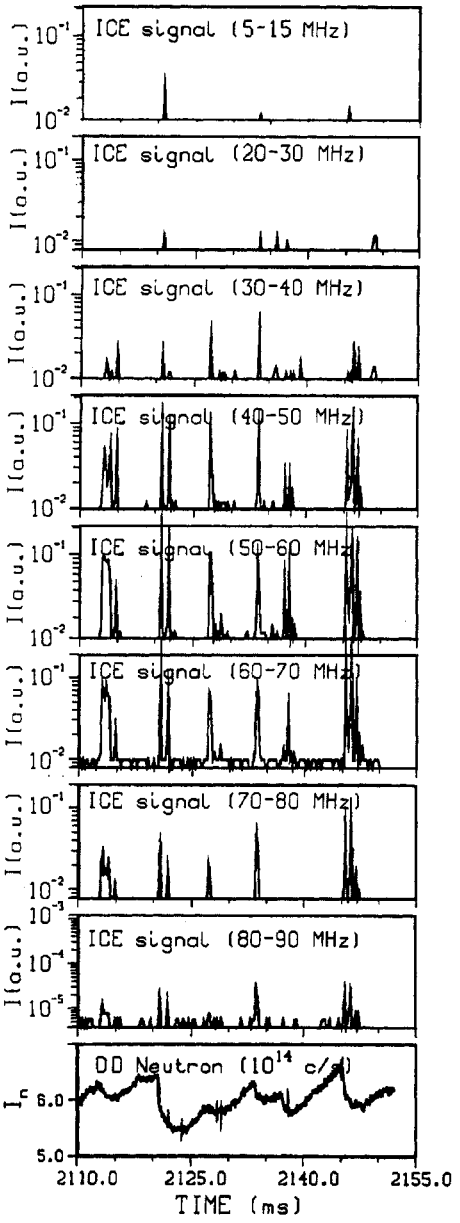

FIG. 17. Time evolution of the ion cyclotron emission and of the neutron emission for a discharge with strong MHD activity. The ICE signal is filtered in several bands (5 up to 90 MHz). Although the ICE signal is seen down to the fundamental frequency (~6.8 MHz at the centre of the plasma and ~5 MHz at the edge), the spectrum actually peaks at a high harmonic. The experiments were conducted at $B_T = 0.9$ MHz, $I_p = 0.7$ MA, $\bar{n}_e = 3 \times 10^{13}$ cm^{-3} and $P_{inj} = 10$ MW.

Edge, fast ion populations were observed to produce ICE in many previous experiments [24, 28–33] and the frequency of the peaks corresponded to the cyclotron frequency of fast ions at the outer edge [24, 28]. Our data closely resemble the ICE measurements during fishbone activity in PDX [24, 29]. Unlike the emission generated by edge fusion products [31], the ICE is virtually synchronous with the TAE burst (Fig. 16), as it was at fishbone bursts in PDX. Another similarity with the PDX observations is that the amplitude is largest for intermediate cyclotron harmonics. The ICE is probably caused by an instability that is driven by beam ions in the edge or scrape-off plasma. Immediately following a burst, the beam distribution function is probably anisotropic and non-monotonic, and the ratio of beam density to plasma density is relatively large. In PBX, ICE was observed during perpendicular injection and not during tangential injection, despite comparable beam ion losses in the two cases [22]. Ion cyclotron emission is also observed in DIII-D discharges with near-tangential injection, where the perpendicular fast ion population is significant; this suggests that perpendicular energy is needed to drive the cyclotron instability.

Theoretically, several loss mechanisms have been suggested. Beam ions that circulate at the mode frequency can experience convective radial transport [34]. This 'mode particle pumping' loss mechanism causes the fast ions to migrate radially outward owing to $\boldsymbol{E} \times \boldsymbol{B}$ drifts. The initial value of the magnetic moment μ is conserved, and the radial velocity is linearly proportional to the mode amplitude $\tilde{B}$. Losses are concentrated near the midplane and occur with a particular phase with respect to the instabilities.

A second resonant loss mechanism is associated with the loss of parallel velocity. With the loss of parallel energy, initially passing particles can become trapped on the inner leg of their orbit and move onto a large, unconfined banana orbit. These unconfined banana orbits collide with the vessel at or below the outer midplane. The losses are predicted to scale linearly with the mode amplitude $\tilde{B}$ [35]. In simulations, this mechanism can dominate alpha losses during TAE modes [35].

A third possible mechanism is orbit stochasticity [35]. This process does not depend upon a resonant interaction with the mode; rather, the helical distortion of the field beats with harmonics of the orbital motion, causing island overlap in phase space. Once island overlap occurs, the particles diffuse rapidly. Transport associated with orbit stochasticity only occurs above a threshold in the mode amplitude. In simulations, the losses scale approximately as $\tilde{B}^2$.

Although all of these effects may play a role in the observed fast ion transport, mode particle pumping seems to be the dominant loss mechanism. The losses inferred from the neutron emission scale linearly with the mode amplitude (Figs 8 and 9), as expected for resonant losses but in contradiction to the scaling expected for orbit stochasticity. To distinguish between mode particle pumping and velocity space transport across the passing–trapped boundary, consider the bolometer data during the limiter scan (Fig. 11). Beam ions that cross the passing–trapped boundary in the plasma interior strike the midplane bolometer with a relatively large pitch angle, $\cos^{-1}(v_\parallel/v)$, of $\sim 52°$. Since these ions move radially about as fast as they do toroidally, orbit calculations indicate that insertion of the limiter into the plasma scrape-off region has little effect upon the expected flux (the limiter was only inserted 6 cm at a distance ~ 700 cm away toroidally). Experimentally, however, the flux decreased by about a factor of two when the limiter was inserted 6 m into the plasma scrape-off region (Fig. 11). This suggests that the lost beam ions spiral out radially with a step size of order 10 cm/pass, rather than suddenly jumping from a confined orbit to an unconfined orbit. The convective radial transport caused by mode particle pumping is qualitatively consistent with the limiter scan data.

In summary, the mode particle pumping theory is consistent with the following features of the data:

(a) The losses scale linearly with mode amplitude (Figs 8 and 9).
(b) The losses are concentrated near the outer midplane (Fig. 11).
(c) The radial step size is of order 10 cm per transit (Fig. 11).
(d) The losses are coherent (Figs 14 and 15).

In PBX, instabilities with many of the features of TAE modes were observed [36 ,37]. Analysis of neutron, charge exchange and diamagnetic loop data during these instabilities suggested that mode particle pumping was also the dominant fast ion loss mechanism in these PBX discharges [37]. For similar mode amplitudes

$$\tilde{B}_\theta/B_T \sim O(10^{-4})$$

the observed reductions in neutron emission on DIII-D are comparable with those on PBX.

Experimentally, the losses tend to be larger during combined fishbone and TAE activity than during either instability alone (Fig. 7). In PBX, combined fishbone and high frequency bursts (which may be related to TAE modes) caused losses that were approximately the sum of the losses associated with either instability alone

[25]. In DIII-D, the combined action of the instabilities tends to be even larger than the sum of the losses normally associated with each mode. One possible explanation for this synergistic effect is that multiple modes cause more island overlap in phase space, enhancing stochastic losses. Another, more likely, explanation is that fishbones resonantly transport beam ions from the plasma centre to outside the $q = 1$ surface, where resonant TAE transport is most effective. (Calculations [6, 38] and measurements [1] of the TAE mode structure in DIII-D indicate that the mode peaks near the $q = 1.5$ surface.)

6. CONCLUSIONS

Our data firmly establish the adverse effect of TAE modes on fast ion confinement. In the presence of violent TAE activity, losses can be as large as 70% of the injected beam power. This is not only a concern for ignition experiments but a potential problem for any experiments with strong external heating by energetic particle injection since beam ions can also excite TAE modes. Measurement of power flux at the first wall indicates that the losses are concentrated near the vessel midplane. In a large scale reactor with high power output, first wall damage resulting from TAE induced fast ion loss is likely. Therefore, it is important that we fully understand TAE stability and develop methods to control the instability. This is the subject of concurrent studies on DIII-D [5] and TFTR. Preliminary results from DIII-D suggest that TAE modes may be stabilized by enhancing continuum damping through the use of current profile control [6] or discharge shaping. Physically, the data suggest that resonant transport is the main loss mechanism. In future work, we plan to install a more extensive set of foil bolometers to provide better poloidal distribution measurements. We also plan to compare the experimental data with realistic theoretical simulations of the fast ion transport.

ACKNOWLEDGEMENTS

The authors thank the entire DIII-D team, especially P.L. Taylor for his continuous support and assistance, C.T. Parker for his assistance with the DIII-D data acquisition system, C.-L. Hsieh and the Thomson group for providing the electron temperature, R. Pinsker and K. Moses for their assistance with the ICE loops, D.N. Hill and R. Ellis for their assistance with the IR cameras, and R. Seraydarian and R.J. Groebner for providing the CER data. Useful discussions with M.S. Chu, C.T. Hsu, L.L. Lao, R. McWilliams, C. Oberman, R. Seraydarian, T.S. Taylor, A.D. Turnbull, K.-L. Wong and S. Zweben are gratefully acknowledged.

This work was supported by General Atomics Subcontract SC120531 under USDOE Contract No. DE-AC03-89ER51114.

REFERENCES

[1] HEIDBRINK, W.W., et al., Nucl. Fusion **31** (1991) 1635.
[2] WONG, K.L., et al., Phys. Rev. Lett. **66** (1991) 1874.
[3] WONG, K.L., et al., Phys. Fluids B **4** (1992) 2122.
[4] DURST, R., et al., Phys. Fluids B **4** (1992) 3707.
[5] STRAIT, E.J., et al., in Plasma Physics and Controlled Nuclear Fusion Research 1992 (Proc. 14th Int. Conf. Würzburg, 1992), Vol. 2, IAEA, Vienna (1993) (in press).
[6] STRAIT, E.J., et al., Stability of Neutral Beam-Driven TAE Modes in DIII-D, Rep. GA-A21037, General Atomics, San Diego (1992) (submitted to Nucl. Fusion).
[7] TURNBULL, A.D., et al., Phys. Fluids B **5** (1993) (in press).
[8] HEIDBRINK, W.W., et al., Phys. Fluids B **5** (1993) (in press).
[9] DARROW, D.S., et al., in Plasma Physics (Proc. 1992 Int. Conf. Innsbruck), Vol. 16C, Part I, European Physical Society (1992) 431.
[10] DUONG, H.H., HEIDBRINK, W.W., Nucl. Fusion **33** (1993) 211.
[11] HEIDBRINK, W.W., SAGER, G., Nucl. Fusion **30** (1990) 1015.
[12] CHENG, C.Z., CHANCE, M.S., Phys. Fluids **29** (1986) 3695.
[13] FU, G.Y., VAN DAM, J.W., Phys. Fluids B **1** (1989) 2404.
[14] FU, G.Y., CHENG, C.Z., Phys. Fluids B **4** (1992) 3722.
[15] BETTI, R., FREIDBERG, J.P., Phys. Fluids B **4** (1992) 1465.
[16] CHENG, C.Z., Phys. Fluids B **3** (1991) 2463.
[17] GORENLENKOV, N.N., SHARAPOV, S.E., Phys. Scr. **45** (1992) 163.
[18] METT, R.R., MAHAJAN, S.M., Phys. Fluids B **4** (1992) 2885.
[19] ROSENBLUTH, M.N., et al., Phys. Rev. Lett. **68** (1992) 596.
[20] ZONCA, F., CHEN, L., Phys. Rev. Lett. **68** (1992) 592.
[21] TOMABECHI, K., in Plasma Physics and Controlled Nuclear Fusion Research 1988 (Proc. 12th Int. Conf. Nice, 1988), Vol. 3, IAEA, Vienna (1989) 215.
[22] HEIDBRINK, W.W., Rev. Sci. Instrum. **57** (1986) 1769.
[23] PETRIE, T.W., SCOVILLE, J.T., Rev. Sci. Instrum. **56** (1985) 1156.
[24] BUCHENAUER, D.A.J., Fast Ion Effects on Magnetic Instabilities in the PDX Tokamak, PhD Thesis, Princeton University, Princeton (1985).
[25] STRACHAN, J.D., et al., Nucl. Fusion **25** (1985) 863.
[26] PFEIFFER, W.W., et al., Nucl. Fusion **25** (1985) 655.

[27] LAO, L.L., et al., Nucl. Fusion **25** (1985) 1611.
[28] TFR GROUP, Nucl. Fusion **18** (1978) 1271.
[29] BHADRA, D.K., et al., Nucl. Fusion **26** (1986) 201.
[30] SEKI, M., et al., Phys. Rev. Lett. **62** (1989) 1989.
[31] SCHILD, P., et al., Nucl. Fusion **29** (1989) 834.
[32] COTTRELL, G.A., et al., in Controlled Fusion and Plasma Heating (Proc. 13th Eur. Conf. Schliersee, 1986), Vol. 10C, Part II, European Physical Society (1986) 37.
[33] GREENE, G.J., TFTR GROUP, in Controlled Fusion and Plasma Heating (Proc. 17th Eur. Conf. Amsterdam, 1990), Vol. 14B, Part IV, European Physical Society (1990) 1540.
[34] WHITE, R.B., et al., Phys. Fluids **26** (1983) 2958.
[35] SIGMAR, D.J., et al., Phys. Fluids B **4** (1992) 1506.
[36] HEIDBRINK, W.W., et al., Phys. Rev. Lett. **57** (1986) 835.
[37] HEIDBRINK, W.W., et al., Phys. Fluids **30** (1987) 1839.
[38] TURNBULL, A.D., et al., in Plasma Physics (Proc. 1992 Int. Conf. Innsbruck), Vol. 16C, Part I, European Physical Society (1992) 435.

(Manuscript received 18 January 1993
Final manuscript received 1 April 1993)